



# Template-free synthesis of polymer-derived mesoporous SiOC/TiO<sub>2</sub> and SiOC/N-doped TiO<sub>2</sub> ceramic composites for application in the removal of organic dyes from contaminated water

Mirabbos Hojamberdiev<sup>a,\*</sup>, Ravi Mohan Prasad<sup>a,\*</sup>, Koji Morita<sup>a,b</sup>, Yongfa Zhu<sup>c</sup>, Marco Antônio Schiavon<sup>d</sup>, Aleksander Gurlo<sup>a</sup>, Ralf Riedel<sup>a</sup>

<sup>a</sup> Fachbereich Material- und Geowissenschaften, Technische Universität Darmstadt, Petersenstr. 32, 64287 Darmstadt, Germany

<sup>b</sup> Fine-grained Refractory Materials Group, Nano Ceramics Center, National Institute for Materials Science, 1-2-1 Sengen, 305 Tsukuba, Japan

<sup>c</sup> Department of Chemistry, Tsinghua University, 100084 Beijing, PR China

<sup>d</sup> Departamento de Ciências Naturais, Universidade Federal de São João Del Rei - UFSJ, 36.301-160 São João Del Rei, MG, Brazil

## ARTICLE INFO

### Article history:

Received 1 November 2011

Received in revised form

19 December 2011

Accepted 22 December 2011

Available online 31 December 2011

### Keywords:

Polymer-derived ceramics

SiOC matrix

Titania

Ceramic composite

Photocatalyst

Nitrogen doping

UV–vis light irradiation

## ABSTRACT

Mesoporous SiOC/TiO<sub>2</sub> and SiOC/N-doped TiO<sub>2</sub> (nitrogen-doped TiO<sub>2</sub>) ceramic composites were prepared by the incorporation of TiO<sub>2</sub> (containing 65 wt.% anatase and 35 wt.% rutile) and N-doped TiO<sub>2</sub> powders into vinyl-functionalized polysiloxane polymer followed by pyrolysis at 700–900 °C for 2 h in argon atmosphere. The N-doped TiO<sub>2</sub> powders were obtained by ammonolysis of commercial TiO<sub>2</sub> nanopowders. The resulting samples were characterized by means of X-ray diffraction, X-ray photoelectron spectroscopy, scanning electron microscopy, transmission electron microscopy and nitrogen physisorption. The specific surface area (*S*<sub>BET</sub>) values of the as-prepared SiOC ceramic and SiOC/TiO<sub>2</sub> and SiOC/N-doped TiO<sub>2</sub> ceramic composites decreased with increasing the pyrolysis temperature due to a gradual collapse of small pores. A transformation from microporous SiOC ceramic (pore-size <2 nm) to mesoporous SiOC/TiO<sub>2</sub> and SiOC/N-doped TiO<sub>2</sub> ceramic composites (pore-size ~4 nm) was analyzed. Adsorption and photocatalytic activity of the resulting samples were evaluated by measuring the decrease in concentration of methylene blue (MB) after adsorption in the dark and photodegradation reaction under UV–vis light irradiation, respectively. Pure microporous SiOC ceramic showed no significant adsorption as well as photocatalytic activity for MB because of its high microporosity and low solid acidity, respectively, whereas mesoporous SiOC/TiO<sub>2</sub> and SiOC/N-doped TiO<sub>2</sub> ceramic composites exhibited higher adsorption and photocatalytic activities. The photodegradation rate constant *k* (× 10<sup>−3</sup> min<sup>−1</sup>) of the samples increased in the following order: 1.3 for SiOC ceramic <2.2 for SiOC/TiO<sub>2</sub> <3.4 for SiOC/N-doped TiO<sub>2</sub>. The highest *k* for the SiOC/N-doped TiO<sub>2</sub> ceramic composite is discussed in terms of the change of the electronic structures and crystallinity of N-doped TiO<sub>2</sub> if compared with pure TiO<sub>2</sub>. These polymer-derived ceramic composites can be applied for the purification of water contaminated with organic dyes without the need for hydrogen peroxide.

© 2011 Elsevier B.V. All rights reserved.

## 1. Introduction

Due to a rapid development of industrial sector, water pollution with organic dyes is a challenging environmental issue in many countries. Because organic dyes are the main constituent of the effluents generated from dyeing industry and are directly discharged

into streams and rivers. Organic dyes are considered as one of the poisonous and harmful compounds for water, soil and human life. Also, they can hinder sunlight's penetration into the water, leading to the eutrophication and the die-off of plants and animals [1]. Hence, there has been an extensive research into developing the system that can remove the molecules of organic dyes from the aquatic environment. Among those methods developed so far, adsorption of organic dyes on porous solids has been found to be an efficient and economic process for the treatment of effluents from dyeing industry [2]. However, most amorphous porous solids having high adsorption ability, due to their high *S*<sub>BET</sub> values, cannot decompose organic dyes because of low solid acidity [3].

With high solid acidity, semiconductor-based photocatalysts have attracted much attention in the last decade because of their

\* Corresponding authors. Tel.: +49 6151 16 6342; fax: +49 6151 16 6346.

E-mail addresses: [hojamberdiev@materials.tu-darmstadt.de](mailto:hojamberdiev@materials.tu-darmstadt.de), [mirabbos.uz@yahoo.com](mailto:mirabbos.uz@yahoo.com) (M. Hojamberdiev), [ravimohan.prasad@gmail.com](mailto:ravimohan.prasad@gmail.com) (R.M. Prasad).

<sup>1</sup> Present address: Materials and Structures Laboratory, Tokyo Institute of Technology, 4259 Nagatsuta, Midori, Yokohama, Kanagawa 226-8502, Japan.

broad range of applications, especially in water purification. Among the oxide semiconductor photocatalysts available up to now, titanium dioxide ( $\text{TiO}_2$ ) has proven to be the most extensively applied one for environmental catalysis because it has a number of advantages, such as excellent photocatalytic activity, comparatively low cost, non-toxicity, biological and chemical inertness; also, it is photostable with near-ultraviolet band gap energy [4]. Because of the wide band gap,  $\text{TiO}_2$  light response is located in the UV region, which accounts for only about 3–5% of the solar energy. To develop efficient visible-light responsive photocatalyst,  $\text{TiO}_2$  was modified by doping metal elements (e.g. Fe, Cr, Co, Mn, Mo, V, Pt, W, etc.), which resulted in the decrease of photocatalytic efficiency owing to thermal instability and increasing carrier trapping [5–9]. Recently, the modification of  $\text{TiO}_2$  with non-metal elements (e.g. B, C, N, S, F and P) has been intensively carried out to extend the photoresponse of  $\text{TiO}_2$  from the UV to the visible-light region [10–16]. Especially, nitrogen doping can provide the possibility to broaden the application of  $\text{TiO}_2$ , such as oxidation of CO, ethanol, gaseous 2-propanol, acetaldehyde,  $\text{NO}_x$  as well as the photodegradation of organic dyes in aqueous solution. The reason for the improvement of photocatalytic activity of  $\text{TiO}_2$  is generally attributed to the decrease of the band gap, which is due to either mixing the N 2p states with O 2p states on the top of the valence band or the creation of N-induced states in the band gap [17]. In addition, the synthesis of mesoporous photocatalysts or the incorporation of oxide photocatalysts in the porous matrices may also allow multiple reflections of UV and visible light within the interior pores that facilitate more efficient use of the light in the photocatalytic process [18]. Besides, high specific surface area ( $S_{\text{BET}}$ ) also provides more active reaction sites and subsequently more accessibility for the reactant to be adsorbed onto the photocatalyst surface and react with the photogenerated electron–hole pairs.

By following the pioneering works on the ordered mesoporous materials with hexagonal and cubic symmetry and pore sizes ranging from 2 to 10 nm [19–22], many families of mesoporous materials (e.g. MCM, SBA, HMS, MSU, FDU, KIT, KSW, HOM, AMS, etc.) with high  $S_{\text{BET}}$  values, tunable pore dimensions and controlled morphologies have been developed so far using different surfactants, co-surfactants and techniques. However, the syntheses of these kinds of mesoporous materials strongly rely on the surfactant micelles and liquid crystals that usually act as templates for the assembly and simultaneous condensation of inorganic precursors, followed by calcination at intermediate temperatures.

Owing to its high  $S_{\text{BET}}$  value, mesoporous silica has found a traditional application for the selective adsorption of various organic dye molecules in water. However, the purely siliceous mesoporous materials have a chemically inert silicate framework and consequently no acid sites [3]; therefore, they cannot be used to decompose the organic adsorbates. As a solid acid having the tendency to donate a proton or to accept an electron pair, undoped and doped  $\text{TiO}_2$  has been combined with mesoporous silica in order to increase its acid strength [23–27], that is, the ability of the surface to convert an adsorbed neutral base into its conjugate acid [28]. The decomposition of the organic dye molecules adsorbed on the titania-immobilized mesoporous silica matrix could be realized under UV- or visible-light illumination. In addition to the enhancement of photocatalytic property, the incorporation of metal oxides or metal oxynitrides into an amorphous mesoporous support with a high  $S_{\text{BET}}$  value also improves thermal and mechanical stability. It was found from the literature survey that the mesoporous photocatalysts and/or in situ synthesized photocatalysts in a porous support demonstrated somehow negligible photocatalytic activities due to the poor degree of crystallinity [29,30]. Normally, a higher degree of crystallinity results in a lower number of crystal defects, decreasing the number of recombination centers for the photogenerated electron–hole pair and increasing the

photocatalytic activity. Therefore, a direct incorporation of highly crystalline photocatalyst nanopowders in the amorphous porous matrix will be a simple way to retain the quantum yield of the photocatalyst.

The pyrolytic transformation of cross-linked preceramic Si-based polymers into the desired ceramic usually results in the release of gaseous by-products that leave behind a variety of pores [31–34]. Particularly, having good mechanical and thermal stability, polymer-derived ceramic products with high  $S_{\text{BET}}$  values and mesoporosity can therefore be considered as potential materials for adsorption and catalyst support [35]. However, using a variety of preceramic polymers, most of mesoporous polymer-derived ceramics were produced on the basis of template (SBA-15, KIT-6, CMK-3 and block copolymers)-assisted method. Therefore, it is still challenging to fabricate ordered mesoporous polymer-derived ceramics without the assistance of templates. Recently, we have demonstrated a direct route for the preparation of polymer-derived mesoporous  $\text{SiOC}/\text{ZnO}$  nanocomposite by a simple incorporation of  $\text{ZnO}$  nanopowders in the vinyl-functionalized polysiloxane followed by pyrolysis at 700 °C for 2 h in argon atmosphere [36] and a template-free self-assembly of  $\text{In}_2\text{O}_3$  nanoparticles to hollow microspheres [37].

In this paper, we report on the novel polymer-derived mesoporous  $\text{SiOC}/\text{TiO}_2$  and  $\text{SiOC}/\text{N}$ -doped  $\text{TiO}_2$  ceramic composites with high  $S_{\text{BET}}$  values and narrow pore size distributions (PSD). To the best of our knowledge, the template-free synthesis of polymer-derived mesoporous  $\text{SiOC}/\text{metal oxynitride}$  ceramic composites was not reported previously. The effects of pyrolysis temperature and  $\text{TiO}_2/\text{N}$ -doped  $\text{TiO}_2$  content on the formation of mesoporous  $\text{SiOC}/\text{TiO}_2$  and  $\text{SiOC}/\text{N}$ -doped  $\text{TiO}_2$  ceramic composites were systematically studied. Adsorption and photodegradation of methylene blue (MB), as a model of organic dye, by the resulting ceramic composites were investigated in the dark and under UV–vis light irradiation, respectively, as functions of pyrolysis temperature and  $\text{TiO}_2/\text{N}$ -doped  $\text{TiO}_2$  content.

## 2. Experimental

### 2.1. Preparation

A commercially available vinyl-functionalized polysiloxane XP RV 200 (Hanse Chemie, Germany) and  $\text{TiO}_2$  nanopowders (Sigma–Aldrich, Germany) with the particle size of less than 100 nm and the  $S_{\text{BET}}$  value of  $\sim 25 \text{ m}^2/\text{g}$  were chosen as preceramic polymer and filler, respectively. As-received  $\text{TiO}_2$  nanopowders contain 65 wt.% anatase and 35 wt.% rutile. In addition, N-doped  $\text{TiO}_2$  powders were also produced by ammonolysis [38] of as-received  $\text{TiO}_2$  nanopowders at 700 °C for 2 h under continuous flow of ammonia gas.

For the preparation of  $\text{SiOC}/\text{TiO}_2$  and  $\text{SiOC}/\text{N}$ -doped  $\text{TiO}_2$  ceramic composites, first, 0.4 g of  $\text{TiO}_2/\text{N}$ -doped  $\text{TiO}_2$  powders was placed in a Schlenk flask and then 1.6 g of vinyl-functionalized polysiloxane XP RV 200 (Fig. 1, as provided by the supplier) was introduced. In order to facilitate the mixing process, 2 ml of anhydrous toluene was dropwise added into the mixture. The mixing process was performed under a magnetic stirring at room temperature for 12 h. The whole mixing process was carried out under purified argon atmosphere. Afterwards, the well-homogenized mixture was transferred into a quartz crucible, and the mixture-containing quartz crucible was then placed in a quartz tube. Pyrolysis of the sample was realized in two steps – initially heated at 200 °C for 2 h to promote a cross-linking process of the polymer and subsequently pyrolyzed at 700–900 °C for 2 h – under a steady flow of argon (50 ml/min) in a programmable horizontal furnace at a heating rate of 50 °C/h. The pyrolysis was completed

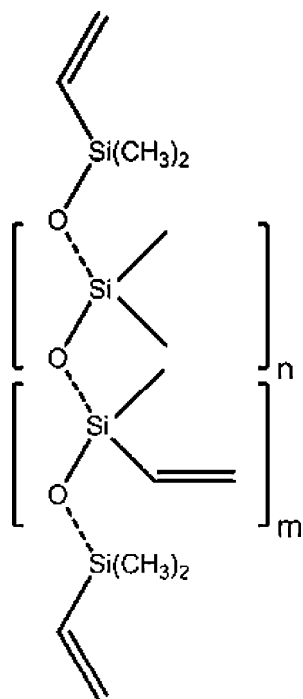


**Fig. 1.** Structure of vinyl-functionalized polysiloxane XP RV 200 (as provided by the supplier).

by cooling the sample to room temperature with a cooling rate of 100 °C/h.

## 2.2. Characterization

To inspect the phase stability of the pyrolyzed samples, X-ray powder diffraction (XRD) characterization was performed in flat-sample transmission geometry on a STADI P X-ray diffractometer (STOE & Cie GmbH, Germany) with Mo K $\alpha$  radiation at a scanning speed of 1° min<sup>-1</sup> in the 2 $\theta$  range of 10–50° and on a D8 Advance diffractometer (Bruker, USA) with Cu K $\alpha$  radiation under reflection scanning mode at a scanning speed of 1° min<sup>-1</sup> in the 2 $\theta$  range of 10–70°. The morphologies of the powdered and bulk samples were examined using a XL30 FEG scanning electron microscope (Philips, The Netherlands) with an acceleration voltage of 15–25 kV. Before the SEM observation, the samples were sputtered with a thin gold layer to avoid charging. Transmission electron microscopy (TEM) measurements were performed on powdered samples using a JEM-2100 instrument (JEOL, Japan) operating at an acceleration voltage of 200 kV in order to distinguish the crystal structure and particle size. For the TEM observation, the powdered sample was dispersed in ethanol using ultrasonic bath, and a small amount of suspension was dropped on the holey carbon grid. Raman spectra were recorded from 100 to 4000 cm<sup>-1</sup> on a confocal Horiba HR800 micro-Raman spectrometer (Horiba Jobin Yvon, Germany) using an excitation laser wavelength of 488 nm. The chemical state and concentration of nitrogen atoms incorporated into the TiO<sub>2</sub> were investigated by X-ray photoelectron spectroscopy (XPS) using an Escalab 250 spectrometer (Thermo VG Scientific, USA) equipped with an Al anode (Al K $\alpha$  = 1486.6 eV). The background pressure in the analysis chamber was lower than 1 × 10<sup>-7</sup> Pa. The measurements were performed using 10 eV pass energy, 0.1 eV step and 0.15 min dwelling time. The UV–vis absorption spectra of the samples were recorded on a Lambda 900 UV/vis/NIR spectrometer (PerkinElmer GmbH, Germany) in the wavelength range of 200–800 nm. The porous properties of the resulting samples were investigated by determining their N<sub>2</sub> adsorption and

desorption isotherms at 77 K using an Autosorb-3B instrument (Quantachrome, USA). The samples were preheated at 150 °C for 12 h under vacuum before the measurement. The specific surface area ( $S_{\text{BET}}$ ) values were calculated by the Brunauer, Emmett and Teller (BET) method [39] from the linear portions of the adsorption isotherms. Pore size distribution (PSD) was calculated by the Barrett, Joyner and Halenda (BJH) method [40] from the desorption branches of isotherms. The total pore volume was calculated from the maximum amount of nitrogen gas adsorption at partial pressure ( $P/P_0$ ) = 0.999.

## 2.3. Adsorption and photocatalytic experiments

Adsorption capacity and photocatalytic activity of the samples were evaluated by measuring the decrease in concentration of MB in the aqueous solution. Aqueous solution of MB (100 ml, 0.03 mM) was placed in a glass vessel, and 50 mg of powdered sample was dispersed. Prior to irradiation, the suspension was magnetically stirred in the dark for 2 h to reach the adsorption–desorption equilibrium. The light was obtained from a 500-W xenon lamp with a quartz glass to simulate the desired irradiation light. During UV–vis light irradiation, 3 ml of aliquot was taken at given time intervals (0, 15, 30, 45, 60, 90 and 120 min) and centrifuged (4000 rpm, 10 min) to remove the solid particles. The supernatants were then analyzed by recording variations of the absorption band maximum ( $\lambda_{\text{max}}$  = 663 nm) in the UV–vis spectra of MB solution by using a U-3010 spectrophotometer (Hitachi, Japan).

## 3. Results and discussion

As confirmed by the XRD patterns of pure and N-doped TiO<sub>2</sub> powders (Fig. 2a), no other phases formed during ammonolysis of commercial TiO<sub>2</sub> nanopowders, i.e. both anatase (JCPDS card no. 21-1272) and rutile (JCPDS card no. 21-1276) phases of titania are retained without significant change in their relative amount and lattice parameters. This indicates that the phase transformation from anatase to rutile is greatly delayed. The broad low intensity reflection at ~43.2° that appears in N-doped TiO<sub>2</sub> can be attributed to one of the titanium suboxides formed in the reducing conditions during the ammonolysis. As Okada et al. [41] demonstrated, the anatase-to-rutile phase transition temperature could be even extended from 680 °C to 1000 °C by the incorporation of 5 mol% of SiO<sub>2</sub>. Our finding is similar to that previously observed by Liu et al. [42] on anatase mechanochemically processed under ammonia atmosphere to produce visible-light sensitive N-doped TiO<sub>2</sub>. It can also be noted that the N-doped TiO<sub>2</sub> sample shows diffraction peaks with slightly higher intensities, evidencing that the heat treatment at 700 °C under ammonia might affect the particle growth of TiO<sub>2</sub> nanopowders.

The UV–vis absorption spectra of pure and N-doped TiO<sub>2</sub> powders are plotted in Fig. 2b. A slight absorbance shift of the N-doped TiO<sub>2</sub> is observed from the UV–vis absorption spectra in comparison to that of commercial TiO<sub>2</sub>. That is, the absorbance to the visible region is slightly extended due to the incorporation of nitrogen. Particularly, a slow increase in optical absorption to the wavelength exceeding 400 nm can be seen. In UV–vis absorption spectrum of the N-doped TiO<sub>2</sub> sample, a significant increase in higher wavelength is still unclear and needs to be studied. Moreover, the absorption intensity of the N-doped TiO<sub>2</sub> is higher than that of commercial TiO<sub>2</sub>. This may be due to the fact that nitrogen occupies some of the oxygen positions in the lattice, and the occupancy of nitrogen in interstitial sites may also give rise to a midgap band between valence and conduction bands. The band gap energies of the samples could be calculated by the formula [43]:  $\alpha h\nu = A(h\nu - E_g)^{n/2}$ , where  $\alpha$ ,  $\nu$ ,  $E_g$ , and  $A$  are the absorption

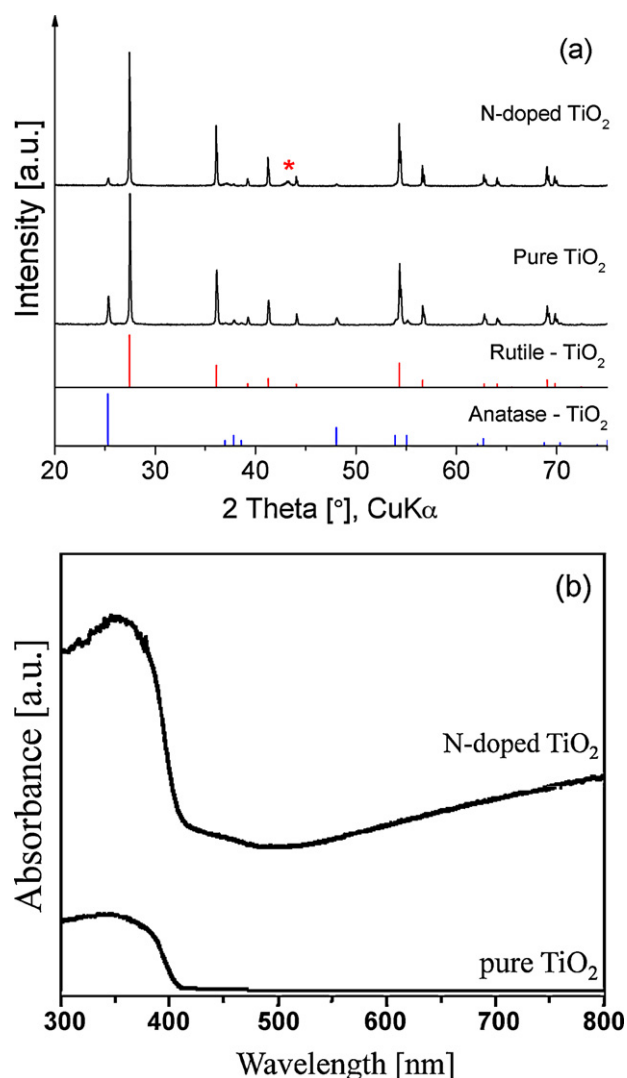


Fig. 2. XRD patterns (a) and UV-vis absorption spectra (b) of pure and N-doped TiO<sub>2</sub> powders. \* – TiO.

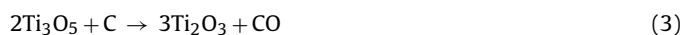
coefficient, light frequency, band gap, and a constant, respectively. The calculated band gap energies for pure and N-doped TiO<sub>2</sub> samples are found to be 3.0 eV and 2.92 eV, respectively. Based on the results from an absorption spectroscopy observation, it can be speculated that the N-doped TiO<sub>2</sub> may have rather higher activity in photodegradation of organic dyes under UV-vis light irradiation.

The SEM micrograph shown in Fig. 3a indicates that commercial TiO<sub>2</sub> nanopowders possess homogenous distribution of tiny particles, whereas the nitrogen doping results in particle agglomeration and growth (Fig. 3b), which is consistent with the XRD and TEM (Fig. 3c and d) results. The TEM micrograph of commercial TiO<sub>2</sub> (Fig. 3c) indicates that the homogeneously distributed TiO<sub>2</sub> nanoparticles have quasi-spherical shape and uniform size in the range of 50–70 nm. The ammonolysis of commercial TiO<sub>2</sub> powders results in the particle aggregation as well as in appearance of irregular shaped particles with the size in the range of 250–400 nm. On the contrary, the synthesis of N-doped TiO<sub>2</sub> through a microemulsion-hydrothermal method indicated that the crystallite size decreased with the increase in N/Ti ratio, without any change in crystal structure [44]. The high resolution transmission electron microscopy (HRTEM) observations (micrographs are not presented here) manifest that the nitrogen doping had no effect on the *d*-spacing value, which indicates that nitrogen was doped

in TiO<sub>2</sub> without changing the average unit cell dimension. The corresponding selected area electron diffraction (SAED) patterns of the samples are shown in the insets of Fig. 3c and d, respectively. These continuous ring-like patterns evidence polycrystallinity in nature and correspond to anatase and rutile phases of TiO<sub>2</sub>, in good agreement with the XRD data.

The chemical state and the concentration of nitrogen atoms in the N-doped TiO<sub>2</sub> were investigated by XPS. As can be seen in Fig. 4a, the XPS survey spectrum of commercial TiO<sub>2</sub> does not include a peak centered at 396 eV. The N 1s XPS spectrum exhibits a broad peak at 396 eV (Fig. 4b) which is characteristic for atomic β-N (interstitial state) substituted for oxygen in N-doped TiO<sub>2</sub> [12] and which is not present in pure TiO<sub>2</sub>. Therefore, the O–Ti–N bonds form in the N-doped TiO<sub>2</sub>. The Ti 2p<sub>3/2</sub> core level spectra of N-doped TiO<sub>2</sub> (not shown here) confirm the incorporation of nitrogen, i.e. the binding energy of Ti 2p<sub>3/2</sub> after nitrogen doping slightly decreases indicating a partial electron transfer from the N<sup>3–</sup> to the Ti<sup>4+</sup> and an increase of the electron density on Ti<sup>4+</sup> (resulting formally in Ti<sup>(4–δ)+</sup>) because of the lower electronegativity of nitrogen compared to oxygen [45]. In the O 1s spectra (not shown here), a shoulder at 532 eV indicates the formation of the Ti–O–N bonds [46,47]. Based on the XPS analysis, the total nitrogen content in the N-doped TiO<sub>2</sub> is calculated to be 1.7 wt.%. Compared with the results of elemental analysis (1.2 wt.% N), the calculated value is slightly higher, which is probably due to the fact that the XPS informs about a surface composition.

Fig. 5a exhibits the results of XRD measurements on the present SiOC/20 wt.% TiO<sub>2</sub> ceramic composite as a function of pyrolysis temperature. The XRD pattern of the SiOC/20 wt.% TiO<sub>2</sub> ceramic composite pyrolyzed at 700 °C for 2 h in argon atmosphere predominantly includes the diffraction peaks of both anatase and rutile. At this pyrolysis temperature, the anatase-to-rutile transformation is retarded even though anatase is metastable at higher temperatures. Upon pyrolysis of the sample at 800 °C for 2 h in argon, the diffraction peaks of anatase completely disappeared with the formation of a new Ti<sub>4</sub>O<sub>7</sub> phase (JCPDS card no. 77-1392) and small amount of remaining rutile. In the XRD pattern of the sample pyrolyzed at 900 °C, the diffraction peaks of rutile phase are completely vanished and the Ti<sub>4</sub>O<sub>7</sub> and Ti<sub>2</sub>O<sub>3</sub> (JCPDS card no. 43-1033) phases start to dominate. We believe that there could be two possible reaction paths for the formation of Ti<sub>4</sub>O<sub>7</sub> phase. On the one hand, owing to the defect and grain boundary concentrations as well as a particle packing, anatase might be transformed to rutile, which was partially consumed subsequently for the formation of the new Ti<sub>4</sub>O<sub>7</sub> phase. On the other hand, both phases might be simultaneously involved in the reaction. Nevertheless, either can be understood in terms of carbothermal reduction of titania. According to the titanium–oxygen phase diagram, loss of oxygen from TiO<sub>2</sub> should result in the formation of a homologous series of lower oxides so-called Magneli phases [48]. These phases have the general formula of Ti<sub>n</sub>O<sub>2n–1</sub> with *n*=4–10, although phases with *n* up to 38 have been reported [49]. Berger [50] observed that the reaction sequence of TiO<sub>2</sub> → Ti<sub>n</sub>O<sub>2n–1</sub> (*n*>10) → Ti<sub>n</sub>O<sub>2n–1</sub> (10 ≥ *n* ≥ 4) → Ti<sub>3</sub>O<sub>5</sub> → Ti<sub>2</sub>O<sub>3</sub> → TiC follows the prediction of the phase diagram. This indicates that large CO evolution occurred during the pyrolysis of the sample and the reduction from TiO<sub>2</sub> to Ti<sub>4</sub>O<sub>7</sub> (the most stable phase), Ti<sub>3</sub>O<sub>5</sub> and Ti<sub>2</sub>O<sub>3</sub> took place:



If the pyrolysis temperature would be further increased, the TiC phase could ultimately form as a lowest series of Magneli phases resulted from the carbothermal reduction of TiO<sub>2</sub>. The Ti<sub>4</sub>O<sub>7</sub> phase has the most negative free energy of reaction, followed by Ti<sub>3</sub>O<sub>5</sub> and



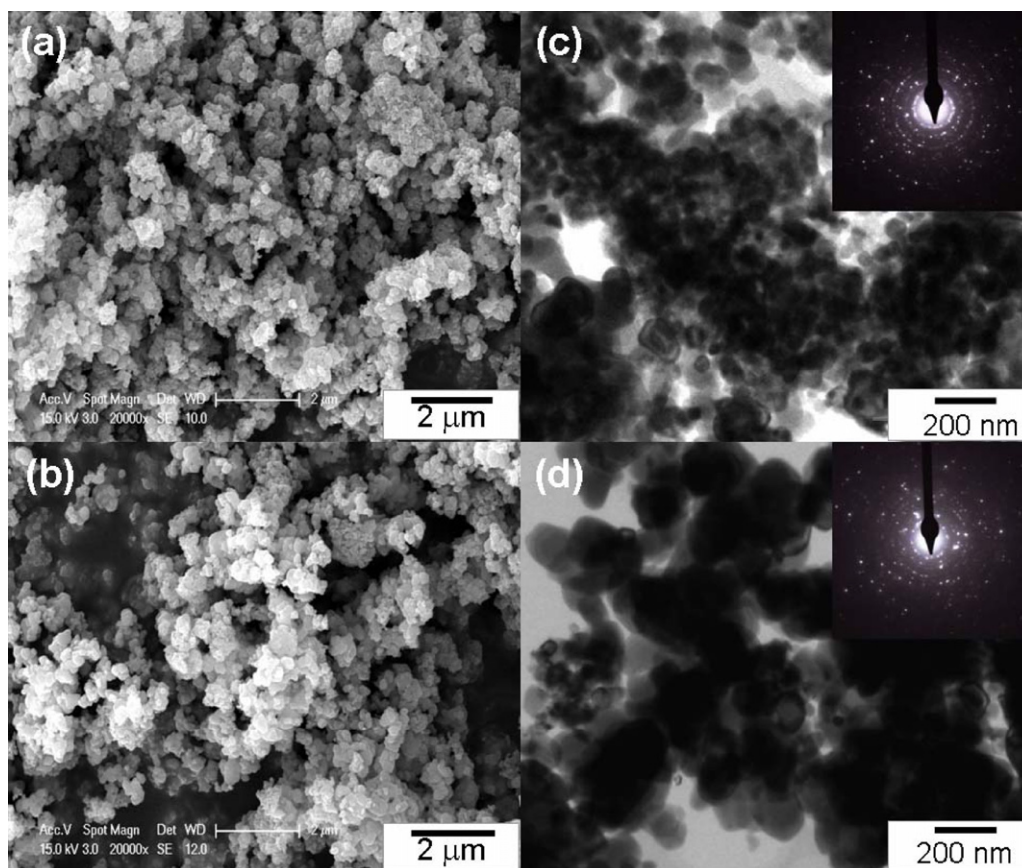


Fig. 3. SEM (a and b) and TEM (c and d) micrographs and SAED patterns (insets) of pure (top) and N-doped (bottom)  $\text{TiO}_2$  powders.

$\text{Ti}_2\text{O}_3$ . Thus, the formation of  $\text{Ti}_4\text{O}_7$  is a thermodynamically favored reaction although the data for the higher Magneli phases were not obtained in our experiments.

Based on the above-given reaction equations, carbon chiefly leads to the continuous reduction of  $\text{TiO}_2$ . Thus, the presence of free carbon phase in the SiOC ceramic pyrolyzed at 700–900 °C for 2 h in argon atmosphere was examined by micro-Raman spectroscopy. The Raman spectra of SiOC ceramic are juxtaposed in Fig. 5b as a function of pyrolysis temperature. As can be seen, the two bands, corresponding to the typical vibration modes in carbonaceous materials, i.e. disordered-induced (D) [51] at 1317  $\text{cm}^{-1}$  and graphitic-like mode [52] at 1546  $\text{cm}^{-1}$ , respectively, appear in the Raman spectrum of the sample pyrolyzed at 800 °C. Intensities of these two bands further increase with increasing pyrolysis temperature up to 900 °C, whereas the sample pyrolyzed at 700 °C does not show any of these bands. That means free-carbon formation was highly promoted at the elevated pyrolysis temperatures.

Fig. 6a shows the XRD patterns of SiOC/ $\text{TiO}_2$  ceramic composite pyrolyzed at 700 °C for 2 h in argon atmosphere as a function of  $\text{TiO}_2$  content. As can be noted, the intensities of the diffraction peaks of anatase and rutile phases increase with the increase in the  $\text{TiO}_2$  content. The XRD patterns confirm that both phases are persistent and no reduction of  $\text{TiO}_2$  at this pyrolysis temperature despite the increased amount of titania.

The XRD patterns of SiOC/20 wt.% N-doped  $\text{TiO}_2$  ceramic composite are shown in Fig. 6b as a function of pyrolysis temperature. Similarly, anatase and rutile phases of titania dominate in the ceramic composite pyrolyzed at 700 °C for 2 h. Quite surprisingly, both anatase and rutile phases are still maintained in the ceramic composite pyrolyzed at 800 °C for 2 h compared to those of SiOC/20 wt.%  $\text{TiO}_2$  ceramic composite pyrolyzed at 800 °C for 2 h.

It seems that the presence of nitrogen in the  $\text{TiO}_2$  has a retarding effect on the transformation from anatase to rutile crystalline phase at this temperature. Since there is an aggregation of  $\text{TiO}_2$  nanoparticles in SiOC/20 wt.% N-doped  $\text{TiO}_2$  ceramic composite (as shown in the TEM micrograph in Fig. 8c), the suppression for the anatase-to-rutile transformation would not be considered as a result of suppressing diffusion between anatase particles in direct contact and limiting their ability to act as surface nucleation sites for rutile [41]. This intriguing phenomenon is still unexplained. Further increase in pyrolysis temperature up to 900 °C for 2 h was not able to further suppress the reduction of  $\text{TiO}_2$ , and so the  $\text{Ti}_4\text{O}_7$  and  $\text{Ti}_2\text{O}_3$  phases formed simultaneously as dominating phases in the SiOC/20 wt.% N-doped  $\text{TiO}_2$  ceramic composite pyrolyzed at 900 °C for 2 h.

The surface morphologies of the samples were examined by scanning electron microscopy (SEM) and the representative micrographs of SiOC ceramic, SiOC/20 wt.%  $\text{TiO}_2$  and SiOC/20 wt.% N-doped  $\text{TiO}_2$  ceramic composites pyrolyzed at 700 °C for 2 h in argon are comparatively shown in Fig. 7. Pure SiOC ceramic possesses a smooth surface with no visible surface features and randomly distributed small debris on the surface of amorphous matrix (Fig. 7a). In contrast to the SiOC ceramic, SiOC/20 wt.%  $\text{TiO}_2$  and SiOC/20 wt.% N-doped  $\text{TiO}_2$  ceramic composites possess unlike surface features with good distribution of  $\text{TiO}_2$  and N-doped  $\text{TiO}_2$  particles in the SiOC matrix (Fig. 7b and c). The size difference in the incorporated particles of  $\text{TiO}_2$  and N-doped  $\text{TiO}_2$  can easily be seen, especially coalescence of N-doped  $\text{TiO}_2$  particles in the SiOC matrix. Evidently, the incorporation of  $\text{TiO}_2$ /N-doped  $\text{TiO}_2$  powders in the polymer under magnetic stirring was sufficient to obtain good-distributed SiOC/20 wt.%  $\text{TiO}_2$  and SiOC/20 wt.% N-doped  $\text{TiO}_2$  ceramic composites.

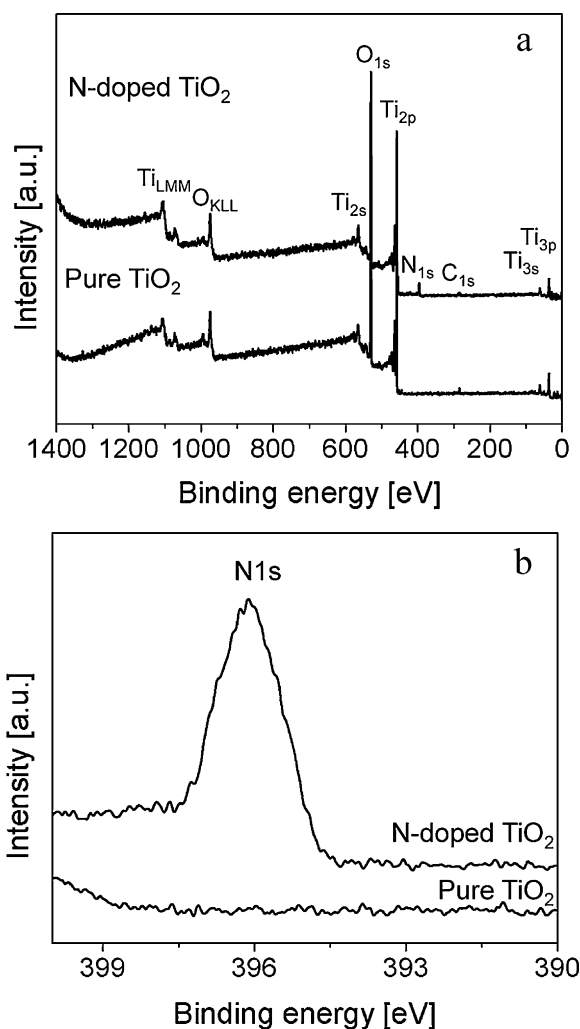


Fig. 4. XPS survey spectra (a) and N 1s XPS spectra (b) of pure and N-doped TiO<sub>2</sub> powders.

TEM was used to further examine the particle size, crystallinity and purity of the as-prepared samples. Fig. 8 displays TEM and HRTEM micrographs and SAED patterns of SiOC ceramic and SiOC/20 wt.% TiO<sub>2</sub> and SiOC/20 wt.% N-doped TiO<sub>2</sub> ceramic composites pyrolyzed at 700 °C for 2 h in argon. Low magnification TEM micrographs of the samples, shown in Fig. 8a–c, confirm the observation from SEM imaging. That is to say, pure SiOC ceramic in Fig. 8a has a plain feature with some randomly distributed small debris of amorphous SiOC, whereas the ceramic composite in Fig. 8b possesses a microstructure clearly revealing fine dispersion of TiO<sub>2</sub> particles <100 nm in the SiOC matrix. In comparison to the SiOC/20 wt.% TiO<sub>2</sub> ceramic composite, the SiOC/20 wt.% N-doped TiO<sub>2</sub> ceramic composite has the agglomeration of N-doped TiO<sub>2</sub> particles, forming larger particles <400 nm dispersed in the SiOC matrix. The SAED in Fig. 8d shows a diffuse ring pattern which is consistent with the amorphous nature of SiOC ceramic. Because amorphous materials normally do not consist of atoms arranged in ordered lattices. In Fig. 8e and f, the SAED patterns of SiOC/20 wt.% TiO<sub>2</sub> and SiOC/20 wt.% N-doped TiO<sub>2</sub> ceramic composites pyrolyzed at 700 °C for 2 h in argon show a set of ring-like patterns instead of regular spots due to the random orientation of crystallites. The identified ring-like patterns correspond to the different planes of polymorphic phases (anatase and rutile) of titania. Similarly, the SAED pattern of spherical titania nanoparticles synthesized through a laser-assisted method also confirms the

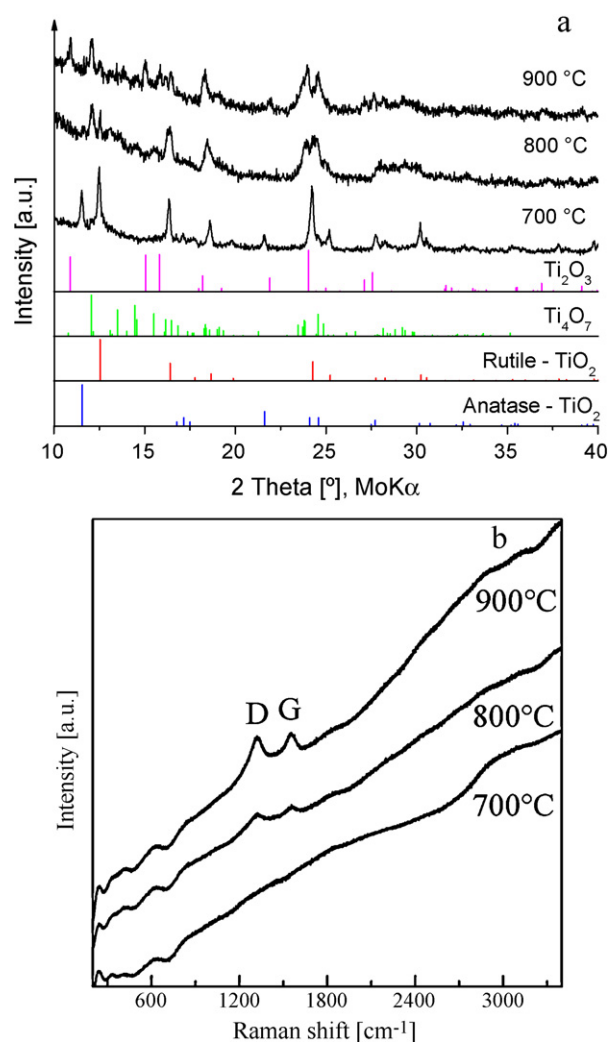
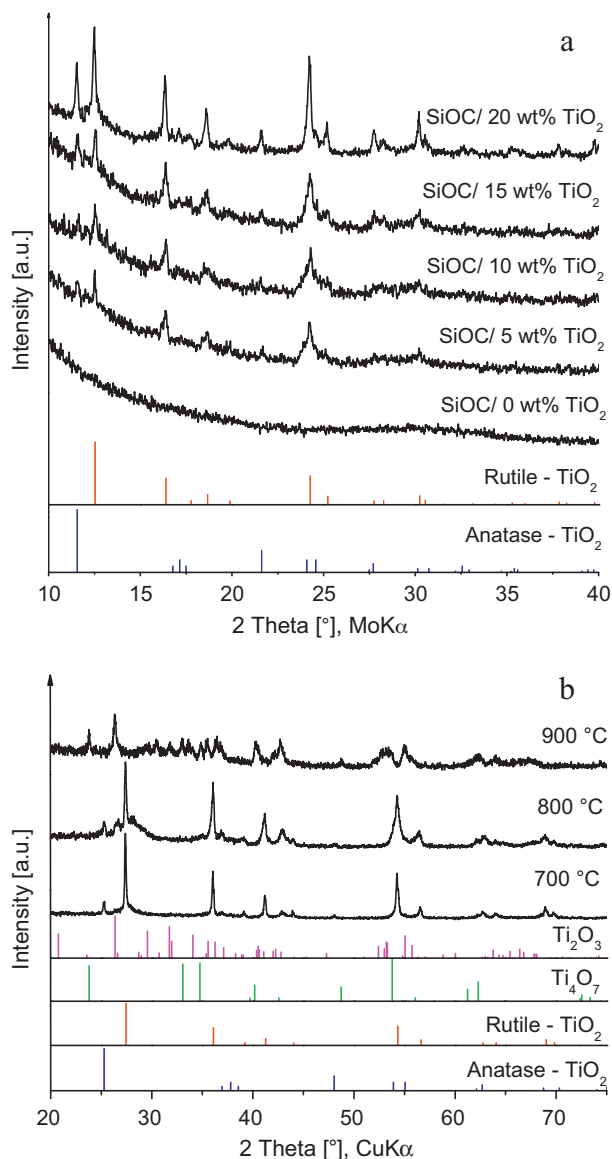


Fig. 5. XRD patterns of SiOC/20 wt.% TiO<sub>2</sub> ceramic composite (a) and Raman spectra of SiOC ceramic (b) as a function of pyrolysis temperature.

formation of anatase and rutile phases [53]. Moreover, the SAED patterns also evidence that there were no phases formed other than incorporated TiO<sub>2</sub>/N-doped TiO<sub>2</sub> having anatase and rutile phases under the current experimental conditions. The HRTEM micrograph of SiOC ceramic shown in Fig. 8g exhibits worm-like microstructural features that are characteristic for the amorphous nature of most Si-based polymer-derived ceramics – absence of lattice-fringe spacings corresponding to turbostratic carbon or other crystalline phases. In short, the overall microstructure of SiOC ceramic pyrolyzed at 700 °C is unlike to those of SiOC ceramics produced at higher temperatures ( $T > 1000$  °C) [54,55]. In the HRTEM micrographs of SiOC/20 wt.% TiO<sub>2</sub> and SiOC/20 wt.% N-doped TiO<sub>2</sub> ceramic composites depicted in Fig. 8h and i, the lattice fringes, encircled by the worm-like microstructural features of the SiOC matrix, with average spacings of 0.352 nm and 0.324 nm are found. These equi-distant parallel lines along can be ascribed to the (1 0 1) plane of anatase and the (1 1 0) plane of rutile, respectively, which are in reasonable agreement with the  $d$  values obtained from the XRD patterns. As mentioned before, the nitrogen doping had no effect on the  $d$ -spacing value, indicating that nitrogen was introduced into the lattice without changing the average unit cell dimension.

Fig. 9a shows the N<sub>2</sub> adsorption–desorption isotherms for the SiOC ceramic and SiOC/20 wt.% TiO<sub>2</sub> and SiOC/20 wt.% N-doped TiO<sub>2</sub> ceramic composites pyrolyzed at 700 °C for 2 h in argon. The



**Fig. 6.** XRD patterns of SiOC/20 wt.%  $\text{TiO}_2$  ceramic composite pyrolyzed at 700 °C for 2 h in argon atmosphere as a function of  $\text{TiO}_2$  content (a) and XRD patterns of SiOC/20 wt.% N-doped  $\text{TiO}_2$  ceramic composite as a function of pyrolysis temperature (b).

adsorption–desorption isotherm of the SiOC ceramic resembles the IUPAC type I isotherm characteristic of micropore adsorption, those of SiOC/20 wt.%  $\text{TiO}_2$  and SiOC/20 wt.% N-doped  $\text{TiO}_2$  ceramic composites – the IUPAC type IV isotherm with single hysteresis loops due to the capillary condensation in mesopores or small micropores [40].

Compared to the adsorption–desorption isotherm of the SiOC ceramic, the adsorption–desorption isotherms of the SiOC/20 wt.%  $\text{TiO}_2$  and SiOC/20 wt.% N-doped  $\text{TiO}_2$  ceramic composites show low adsorption in the  $P/P_0$  range of 0–0.8 but increases continuously and raises very steeply at  $P/P_0 = 0.8$ –1.0. In contrast, desorption branches of the adsorption–desorption isotherms of the ceramic composites show a pronounced step around  $P/P_0 = 0.5$  resulting in the closure of the hysteresis loops. The maximum nitrogen adsorption is higher in SiOC/20 wt.%  $\text{TiO}_2$  compared to that of SiOC/20 wt.% N-doped  $\text{TiO}_2$  ceramic composite probably due to an increase in the particle size distribution after ammonolysis of commercial  $\text{TiO}_2$  nanopowders.

By the incorporation of  $\text{TiO}_2$ /N-doped  $\text{TiO}_2$  powders into the polymer followed by pyrolysis, microporous pure SiOC was

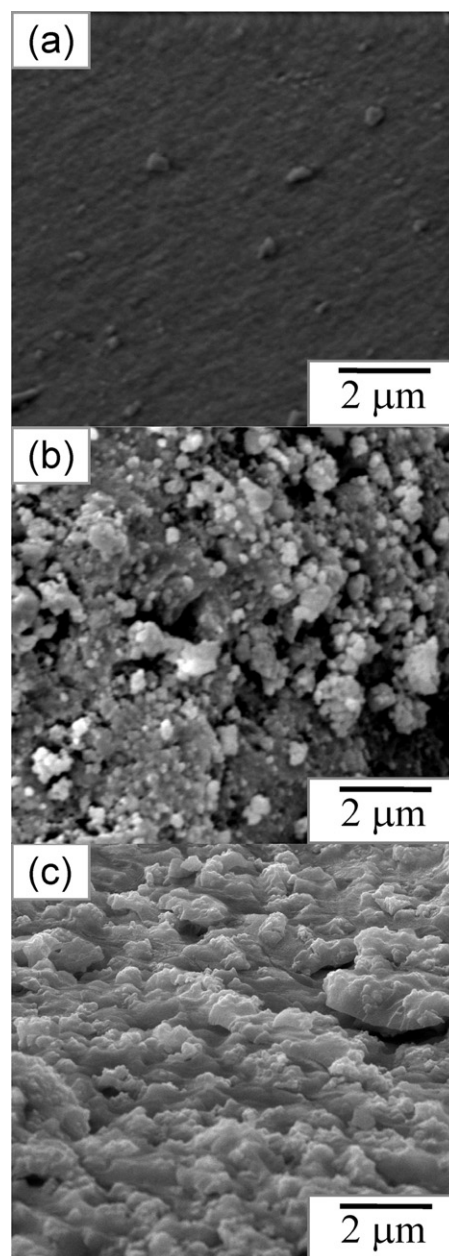


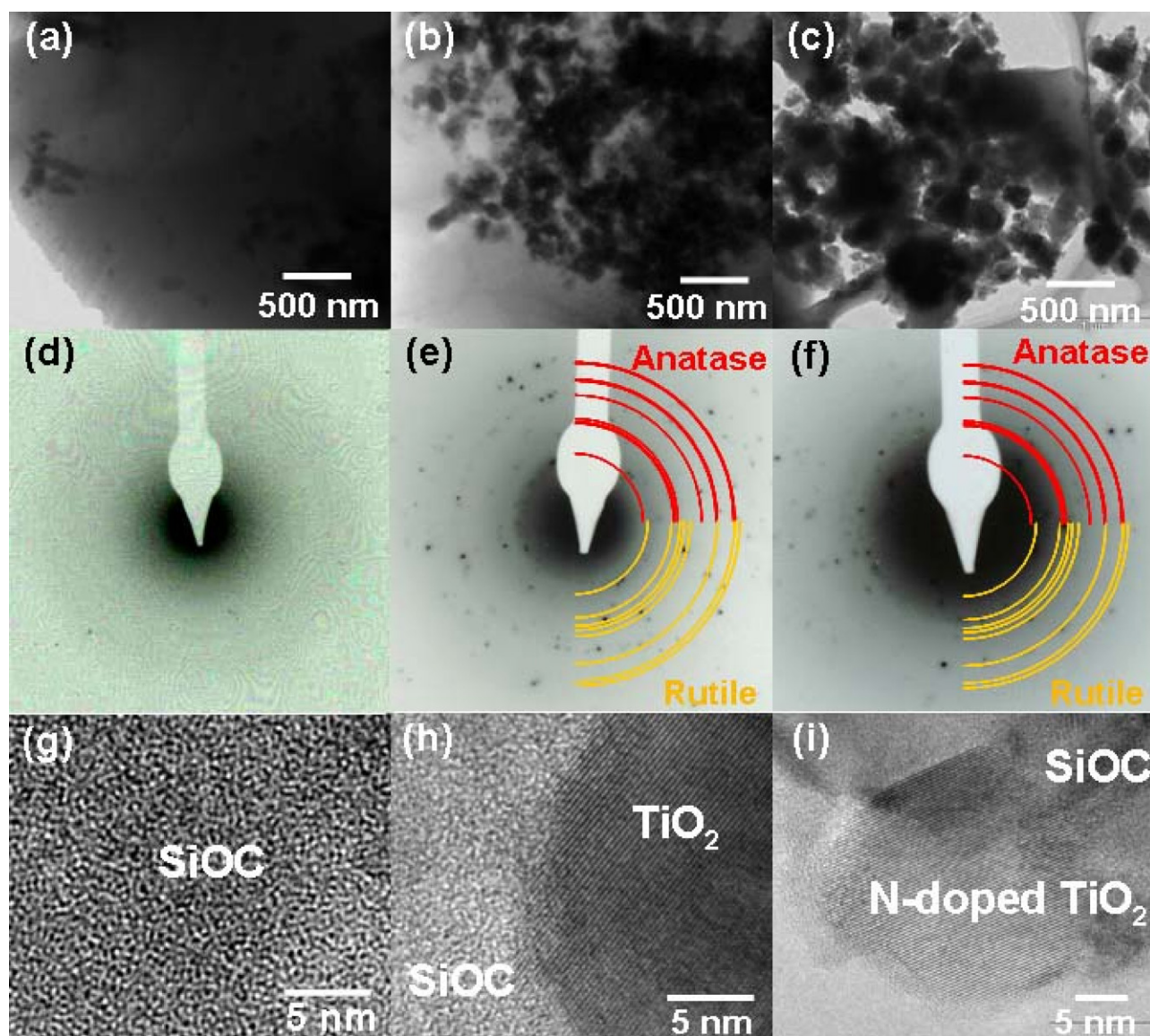
**Fig. 7.** SEM micrographs of SiOC ceramic (a) and SiOC/20 wt.%  $\text{TiO}_2$  (b) and SiOC/20 wt.% N-doped  $\text{TiO}_2$  (c) ceramic composites pyrolyzed at 700 °C for 2 h in argon atmosphere.

transformed to mesoporous SiOC/20 wt.%  $\text{TiO}_2$  and SiOC/20 wt.% N-doped  $\text{TiO}_2$  ceramic composites. This is thought to be due mainly to the result of the structural rearrangement of the polymer (polymer chains) with the addition of  $\text{TiO}_2$ /N-doped  $\text{TiO}_2$  powders. However, an exact mechanism for the microposity-to-mesoporosity transformation is not fully understood yet. Fig. 9b shows the corresponding PSDs, calculated based on the desorption branches of isotherms, of the SiOC ceramic and SiOC/20 wt.%  $\text{TiO}_2$  and SiOC/20 wt.% N-doped  $\text{TiO}_2$  ceramic composites pyrolyzed at 700 °C for 2 h in argon. As can be seen, a micropore peak at <2 nm in the PSD curve of the SiOC ceramic imperfectly shifts to mesopore peaks at about 3.9 nm and 3.9 and 4.2 nm in the PSD curves of the SiOC/20 wt.%  $\text{TiO}_2$  and SiOC/20 wt.% N-doped  $\text{TiO}_2$  ceramic composites, respectively. However, a mixture of mesopores (>4 nm in pore diameter) and micropores (<2 nm in pore diameter) can also be noted in the PSD curves of the ceramic composites. Interestingly, SiOC/20 wt.%



**Table 1**  
Porous properties of the samples.

Sample	Pyrolysis temperature (°C)	TiO <sub>2</sub> /N-doped TiO <sub>2</sub> powders (wt.%)	S <sub>BET</sub> (m <sup>2</sup> /g)	Pore type	Pore volume (ml/g)
SiOC ceramic	700	–	398	Micro	0.08
	800	–	248	Micro	0.05
	900	–	60	Micro	0.05
SiOC/TiO <sub>2</sub> ceramic composite	700	20	336	Meso/micro	0.27
	800	20	256	Meso/micro	0.26
	900	20	212	Meso/micro	0.05
SiOC/TiO <sub>2</sub> ceramic composite	700	0	398	Micro	0.08
	700	5	382	Meso/micro	0.08
	700	10	365	Meso/micro	0.10
	700	15	351	Meso/micro	0.12
	700	20	336	Meso/micro	0.27
SiOC/N-doped TiO <sub>2</sub> ceramic composite	700	20	254	Meso/micro	0.17
	800	20	157	Meso/micro	0.16
	900	20	129	Meso/micro	0.05

**Fig. 8.** TEM micrographs (a–c), SAED patterns (d–f) and HRTEM micrographs (g–i) of SiOC ceramic (left) and SiOC/20 wt.% TiO<sub>2</sub> (middle) and SiOC/20 wt.% N-doped TiO<sub>2</sub> (right) ceramic composites pyrolyzed at 700 °C for 2 h in argon atmosphere.



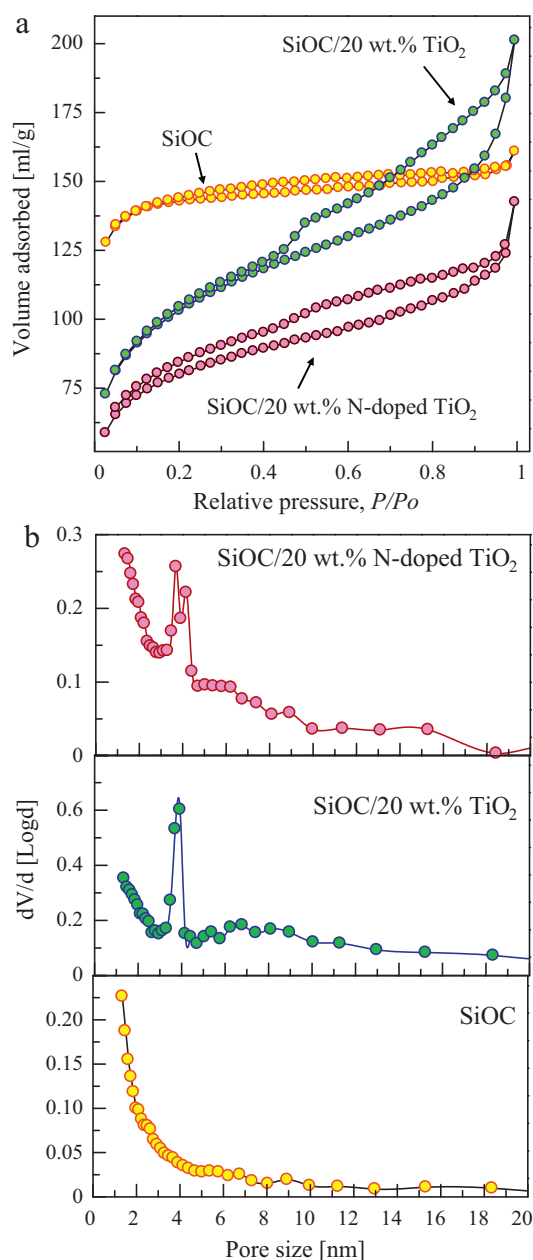


**Fig. 9.** N<sub>2</sub> adsorption-desorption isotherms (a) and pore size distributions (b) of SiOC ceramic and SiOC/20 wt.% TiO<sub>2</sub> and SiOC/20 wt.% N-doped TiO<sub>2</sub> ceramic composites pyrolyzed at 700 °C for 2 h in argon atmosphere.

N-doped TiO<sub>2</sub> ceramic composite has more microporosity compared to that of SiOC/20 wt.% TiO<sub>2</sub>. Probably, the larger particle size of N-doped TiO<sub>2</sub> powders had less interaction with the polymer chains that led to the formation of more micropores. Nevertheless, the PSD curves of the samples justify the transformation from microporous SiOC ceramic to mesoporous SiOC/20 wt.% TiO<sub>2</sub> and SiOC/20 wt.% N-doped TiO<sub>2</sub> ceramic composites. Table 1 summarizes the porosity features, viz. the  $S_{\text{BET}}$  value, total pore volume and pore type, of SiOC ceramic and SiOC/20 wt.% TiO<sub>2</sub> and SiOC/20 wt.% N-doped TiO<sub>2</sub> ceramic composites as functions of pyrolysis temperature and TiO<sub>2</sub>/N-doped TiO<sub>2</sub> content. The increase in pyrolysis temperature from 700 °C to 900 °C reduces the  $S_{\text{BET}}$  values monotonically for all the samples. That is, the  $S_{\text{BET}}$  value decreases from 398 m<sup>2</sup>/g to 60 m<sup>2</sup>/g in SiOC ceramic, from 336 m<sup>2</sup>/g to 212 m<sup>2</sup>/g in SiOC/20 wt.% TiO<sub>2</sub> ceramic composite and from 254 m<sup>2</sup>/g to 129 m<sup>2</sup>/g in SiOC/20 wt.% N-doped TiO<sub>2</sub> ceramic composite due

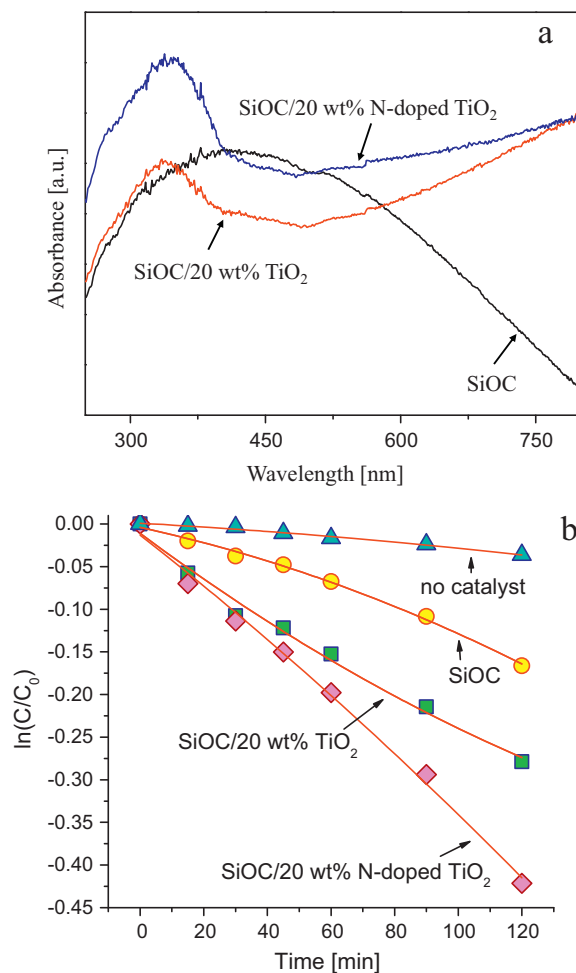


**Fig. 10.** UV-vis absorption spectra (a) and photocatalytic activity (b) of SiOC ceramic and SiOC/20 wt.% TiO<sub>2</sub> and SiOC/20 wt.% N-doped TiO<sub>2</sub> ceramic composites pyrolyzed at 700 °C for 2 h in argon atmosphere.

to a gradual collapse of small pores. Note that the  $S_{\text{BET}}$  values in SiOC/20 wt.% N-doped TiO<sub>2</sub> ceramic composite are lower than those in SiOC/20 wt.% TiO<sub>2</sub> ceramic composite. For this, the reason might be the initial particle size of filler which might have had a pronounced impact on the formation of higher  $S_{\text{BET}}$  values. With increasing the TiO<sub>2</sub> amount from 0% to 20% in the polymer, the  $S_{\text{BET}}$  value decreases from 398 m<sup>2</sup>/g to 336 m<sup>2</sup>/g in the SiOC/TiO<sub>2</sub> ceramic composite. In comparison to those of the ceramic composites, the  $S_{\text{BET}}$  value in SiOC ceramic reduces abruptly with increasing pyrolysis temperature. Here, it can be concluded that the incorporation of TiO<sub>2</sub>/N-doped TiO<sub>2</sub> powders in the pure SiOC matrix maintains the  $S_{\text{BET}}$  and strengthens the porous structure against a gradual collapse at the elevated pyrolysis temperature, which are beneficial for photocatalytic reaction. The total pore volume decreases monotonically in the samples with the increase in pyrolysis temperature and increases in SiOC/20 wt.% TiO<sub>2</sub> ceramic composite with the increase in the TiO<sub>2</sub> content.

Fig. 10a shows UV-vis absorption spectra of SiOC ceramic and SiOC/20 wt.% TiO<sub>2</sub> and SiOC/20 wt.% N-doped TiO<sub>2</sub> ceramic composites pyrolyzed at 700 °C for 2 h in argon atmosphere. The absorption spectrum of SiOC ceramic shows no distinct absorption band in the wavelength range of 200–800 nm, instead one broad shallow peak. In amorphous semiconductors showing similar absorption peak, the absence of sharp band gap edges, localization of states in energy regions and the existence of broad bands of defect levels in the gap were found [56]. In contrast, SiOC/20 wt.% TiO<sub>2</sub> and SiOC/20 wt.%

N-doped TiO<sub>2</sub> ceramic composites show almost the same absorption edge as TiO<sub>2</sub> and N-doped TiO<sub>2</sub> powders (shown in Fig. 2b) at above 400 nm with lower intensity but extended the absorbance to the whole visible region. As expected, the intensity of absorption in the UV–vis region is higher in SiOC/20 wt.% N-doped TiO<sub>2</sub> ceramic composites. Owing to the presence of amorphous SiOC matrix, the incorporation of crystalline oxide powders into the SiOC matrix might increase a surface electric charge of the oxide in the ceramic composites that may lead to the modification of electron-hole pair formation process [57].

Titanium exists as three different polymorphs: rutile (tetragonal), anatase (tetragonal) and brookite (orthorhombic). Rutile is thermodynamically stable, while anatase and brookite are metastable, transforming to rutile at elevated temperatures, typically at 600–700 °C [58]. Anatase is usually considered to be the most photoactive of the three polymorphs for the degradation of organic pollutants [59]. Recently, it was found that the mixed anatase–rutile phases of titania even present the highest activity for the photodegradation of organic dye molecules due mainly to the following three factors, as Hurum et al. [60] described: (1) smaller band gap of rutile extends the useful range of photoactivity into visible region, (2) stabilization of charge separation by electron transfer from rutile and anatase slows recombination rate, and (3) catalytic hot spots at the rutile/anatase interface. In this connection, commercial TiO<sub>2</sub> nanopowders containing 65 wt.% anatase and 35 wt.% rutile was therefore applied in this study.

To explore the potential of new ceramic composites for application in the removal of organic dyes from contaminated water, adsorption and photocatalytic degradation of MB, as a representative of water polluting organic dyes in the textile effluent, in aqueous solution by the as-prepared samples were performed in the dark and under UV–vis light irradiation, respectively.

Prior to UV–vis light irradiation, the reaction system was kept in the dark for 2 h to insure sufficient adsorption of MB molecules on the surfaces of the samples. From the experiments, it was evident that the samples with higher  $S_{\text{BET}}$  values and higher mesoporosity showed higher adsorption capacity. The capacity of the samples for the MB adsorption decreased in the following order: SiOC/20 wt.% TiO<sub>2</sub> > SiOC/20 wt.% N-doped TiO<sub>2</sub> > SiOC. It is worth noting that pure SiOC ceramic with the highest  $S_{\text{BET}}$  value shows an opposite trend, i.e. the lowest adsorption capacity because of high volume of microporosity. This is because the MB molecule has a minimum molecular cross-sectional diameter of about 0.8 nm, and it has been estimated that to allow MB molecule to access the minimum pore diameter should be 1.3 nm [61]. Indeed, SiOC ceramic shows some adsorption due to the presence of only largest micropores. Additionally, the nitrogen doping also enhanced MB adsorption although SiOC/20 wt.% N-doped TiO<sub>2</sub> ceramic composite has larger particles and comparatively lower  $S_{\text{BET}}$  value, which may generally cause lower absorption. Previous study [62] reported that the surface zeta potential of the N-doped TiO<sub>2</sub> is more negative than that of pure TiO<sub>2</sub>. Since the MB ions are positively charged in water, they are easily adsorbed onto the negatively charged surface of the N-doped TiO<sub>2</sub> in the SiOC matrix.

The photodegradation rate constant has been chosen as the basic kinetic parameter to compare the photocatalytic activity of the as-prepared samples, since it enables to determine photocatalytic activity independent to the adsorption period in the dark and the MB concentration remaining in the solution [63]. Hence, the Langmuir–Hinshelwood kinetic model, the first order kinetic equation  $\ln(C/C_0) = -k \cdot t$ , was used to fit the experimental data, where  $k$  is the photodegradation rate constant,  $C$  is the MB concentration at time  $t$ , and  $C_0$  is the initial MB concentration at  $t=0$ . In time profiles of  $\ln(C/C_0)$  under UV–vis light irradiation shown in Fig. 10b, the  $\ln(C/C_0)$  linearly decreases, which means the photodegradation of MB over these samples could be described as a

first-order reaction. The photocatalytic activity of samples can be evaluated by using the value of  $k$ , i.e. the bigger the value of  $k$ , the higher the photocatalytic activity. The photodegradation rate constant  $k (\times 10^{-3} \text{ min}^{-1})$  increases in the following order: 1.3 for SiOC ceramic < 2.2 for SiOC/TiO<sub>2</sub> < 3.4 for SiOC/N-doped TiO<sub>2</sub>. An additional photodegradation experiments were performed with pure TiO<sub>2</sub> and N-doped TiO<sub>2</sub>. The photodegradation rate constants of pure TiO<sub>2</sub> and N-doped TiO<sub>2</sub> are estimated to be  $8.7 \times 10^{-3} \text{ min}^{-1}$  and  $27 \times 10^{-3} \text{ min}^{-1}$ , respectively. The highest  $k$  for SiOC/N-doped TiO<sub>2</sub> ceramic composite may be attributed to the change of the electronic structures and crystallinity of TiO<sub>2</sub> with nitrogen doping. In SiOC/TiO<sub>2</sub> ceramic composite, in addition to the homogeneously dispersed TiO<sub>2</sub> nanoparticles, the large  $S_{\text{BET}}$  value also facilitates the adsorption and utilization of light and offers more active sites for photocatalysis. As Wang et al. [64] demonstrated, a proper conformation of pores allows light waves to penetrate inside the catalyst deeply and leads to high mobility of photogenerated charges. It is believed that in the total MB photodegradation mechanism, adsorption of MB onto the surfaces of the samples took place first, and then the MB-occupied TiO<sub>2</sub> particles were excited under UV–vis light irradiation to generate hydroxyl and superoxide radicals, and finally both radicals decomposed the adsorbed MB molecules.

The fact above demonstrates that the SiOC/N-doped TiO<sub>2</sub> ceramic composite pyrolyzed at 700 °C for 2 h in argon shows an enhanced photocatalytic activity than pure SiOC ceramic and SiOC/TiO<sub>2</sub> ceramic composite. This enhancement can be due to the doping effect of nitrogen, allowing TiO<sub>2</sub> to be excited under UV–vis light irradiation. Because it has a comparatively reduced band gap and it can have higher photo-generated holes and electrons. Moreover, there might have been involved some other processes, as several research groups have so far discussed the origin of the visible-light response of N-doped TiO<sub>2</sub>. For instance, Asahi et al. [12] considered that a visible-light response arose from band narrowing by mixing of N2p and O2p orbitals. Irie et al. [65] suggested that that might be owing to an isolated impurity levels above the valence band. Lindgren et al. [66] attributed it to the close situation of N2p to the valence band, instead the conduction band was remained unchanged. Ihara et al. [67] reported that a visible-light response was contributed by the stabilization of oxygen vacancies formed in the grain boundaries by nitrogen doping. The obtained results highlight that the direct incorporation of photocatalytically active nanoparticles of TiO<sub>2</sub> and N-doped TiO<sub>2</sub> into a polymer-derived amorphous SiOC matrix is a promising strategy for designing new heterogeneous photocatalysts.

#### 4. Conclusions

Polymer-derived mesoporous SiOC/TiO<sub>2</sub> and SiOC/N-doped TiO<sub>2</sub> ceramic composites were prepared by the incorporation of TiO<sub>2</sub> (containing 65 wt.% anatase and 35 wt.% rutile) and N-doped TiO<sub>2</sub> powders into vinyl-functionalized polysiloxane polymer followed by pyrolysis at 700–900 °C for 2 h in argon atmosphere. The following results were obtained from this study:

- (1) The pyrolysis temperature had a strong influence on the phase stability of TiO<sub>2</sub> and N-doped TiO<sub>2</sub> powders incorporated in the SiOC matrix. Pure TiO<sub>2</sub> was phase-stable only at pyrolysis temperature of 700 °C while N-doped TiO<sub>2</sub> was up to 800 °C due to the incorporation of nitrogen.
- (2) The growth of N-doped TiO<sub>2</sub> particles after ammonolysis of commercial TiO<sub>2</sub> nanopowders, good distribution of the incorporated TiO<sub>2</sub> and N-doped TiO<sub>2</sub> powders in the SiOC matrix and absence of impurity phases were noted in the as-prepared samples.

- (3) The  $S_{\text{BET}}$  values of the as-prepared SiOC ceramic and SiOC/TiO<sub>2</sub> and SiOC/N-doped TiO<sub>2</sub> ceramic composites decreased with increasing the pyrolysis temperature due to a gradual collapse of small pores. A transformation from microporous SiOC ceramic (pore-size <2 nm) to mesoporous SiOC/TiO<sub>2</sub> and SiOC/N-doped TiO<sub>2</sub> ceramic composites (pore-size ~4 nm) was observed.
- (4) Pure microporous SiOC ceramic showed no significant adsorption and photocatalytic activity for MB degradation due to its high microporosity and low solid acidity, respectively, whereas mesoporous SiOC/TiO<sub>2</sub> and SiOC/N-doped TiO<sub>2</sub> ceramic composites exhibited higher adsorption and higher photocatalytic activity.
- (5) The synergetic effects of higher  $S_{\text{BET}}$  value and higher mesoporosity of the samples caused an increase in adsorption of MB. The photodegradation rate constant  $k$  ( $\times 10^{-3} \text{ min}^{-1}$ ) increased in the following order: 1.3 for SiOC <2.2 for SiOC/TiO<sub>2</sub> <3.4 for SiOC/N-doped TiO<sub>2</sub>. The highest  $k$  for SiOC/N-doped TiO<sub>2</sub> ceramic composite may be attributed to the change of the electronic structures and crystallinity of N-doped TiO<sub>2</sub>.

## Acknowledgments

MH would like to thank the Alexander von Humboldt (AvH) Stiftung for the award of a postdoctoral research fellowship under which the present study was carried out. The authors wish to thank Dr. Gabriela Mera and Dipl.-Ing. René Hock for performing micro-Raman spectroscopy and X-ray photoelectron spectroscopy (XPS) measurements, respectively.

## References

- [1] N. Buvanewari, C. Kannan, J. Hazard. Mater. 189 (2011) 294–300.
- [2] R.C. Bansal, M. Goyal, Activated Carbon Adsorption, CRC Press, Boca Raton, FL, 2005.
- [3] T. Linssen, F. Mees, K. Cassiers, P. Cool, A. Whittaker, E.F. Vansant, J. Phys. Chem. B 107 (2003) 8599–8606.
- [4] R.J. Tayade, R.G. Kulkarni, R.V. Jasra, Ind. Eng. Chem. Res. 46 (2007) 369–376.
- [5] J.F. Zhu, F. Chen, J.L. Zhang, H.J. Chen, M. Anpo, J. Photochem. Photobiol. A 180 (2006) 196–204.
- [6] D. Dvoranová, V. Brezová, M. Mazúr, M.A. Malati, Appl. Catal. B 37 (2002) 91–105.
- [7] Y.-H. Chen, M. Franzreb, R.-H. Lin, L.-L. Chen, C.-Y. Chang, Y.-H. Yu, P.-C. Chiang, Ind. Eng. Chem. Res. 48 (2009) 7616–7623.
- [8] A. Di Paola, G. Marci, L. Palmisano, M. Schiavella, K. Uosaki, S. Ikeda, B. Ohtani, J. Phys. Chem. B 106 (2002) 637–645.
- [9] J. Zhu, Z. Deng, F. Chen, J. Zhang, H. Chen, M. Anpo, J. Huang, L. Zhang, Appl. Catal. B 62 (2006) 329–335.
- [10] W. Zhao, W. Ma, C. Chen, J. Zhao, Z. Shuai, J. Am. Chem. Soc. 126 (2004) 4782–4783.
- [11] S. Sakthivel, H. Kisch, Angew. Chem. Int. Ed. 42 (2003) 4908–4911.
- [12] R. Asahi, T. Morikawa, T. Ohwaki, K. Aoki, Y. Taga, Science 293 (2001) 269–271.
- [13] S. Sato, R. Nakamura, S. Abe, Appl. Catal. A 284 (2005) 131–137.
- [14] J.C. Yu, W. Ho, J. Yu, H. Yip, P.K. Wong, J. Zhao, Environ. Sci. Technol. 39 (2005) 1175–1179.
- [15] J.C. Yu, J. Yu, W. Ho, Z. Jiang, L. Zhang, Chem. Mater. 14 (2002) 3808–3816.
- [16] L. Korosi, I. Dekany, Colloids Surf. A 280 (2006) 146–154.
- [17] O. Diwald, T.L. Thompson, T. Zubkov, Ed.G. Goralski, S.D. Walck, J.T. Yates Jr., J. Phys. Chem. B 108 (2004) 6004–6008.
- [18] H. Li, Z. Bian, J. Zhu, D. Zhang, G. Li, Y. Huo, H. Li, Y. Lu, J. Am. Chem. Soc. 129 (2007) 8406–8407.
- [19] T. Yanagisawa, T. Shimizu, K. Kuroda, C. Kato, Bull. Chem. Soc. Jpn. 63 (1990) 988–992.
- [20] C.T. Kresge, M.E. Leonowicz, W.J. Roth, J.C. Vartuli, J.S. Beck, Nature 359 (1992) 710–712.
- [21] J.S. Beck, J.C. Vartuli, W.J. Roth, M.E. Leonowicz, C.T. Kresge, K.D. Schmitt, C.T.W. Chu, D.H. Olson, E.W. Sheppard, J. Am. Chem. Soc. 114 (1992) 10834–10843.
- [22] J.C. Vartuli, K.D. Schmitt, C.T. Kresge, W.J. Roth, M.E. Leonowicz, S.B. McCullen, S.D. Hellring, J.S. Beck, J.L. Schlenker, Chem. Mater. 6 (1994) 2317–2326.
- [23] K. Okada, A. Yoshizawa, Y. Kameshima, T. Isobe, A. Nakajima, K.J.D. Mackenzie, J. Porous Mater. 18 (2011) 345–354.
- [24] M. Tasbihi, U.L. Štangar, U. Černigoj, J. Jirkovsky, S. Bakardjieva, N.N. Tušar, Catal. Today 161 (2011) 181–188.
- [25] S. Shen, Y. Deng, G. Zhu, D. Mao, Y. Wang, G. Wu, J. Li, X. Liu, G. Lu, D. Zhao, J. Mater. Sci. 42 (2007) 7057–7061.
- [26] H. Yang, Y. Deng, C. Du, Colloids Surf. A 339 (2009) 111–117.
- [27] M. Gohin, I. Maurin, T. Gacoin, J.-P. Boilot, J. Mater. Chem. 20 (2010) 8070–8077.
- [28] K. Tanabe, M. Misono, Y. Ono, H. Hattori, New Solid Acids and Bases and Their Catalytic Properties, Elsevier, Amsterdam, 1989, p. 5.
- [29] D.S. Kim, S.-Y. Kwak, Appl. Catal. A 323 (2007) 110–118.
- [30] S.X. Ren, X. Zhao, L.N. Zhao, M.R. Yuan, Y. Yu, Y.P. Guo, Z.C. Wang, J. Solid State Chem. 182 (2009) 312–316.
- [31] P. Colombo, Science 322 (2008) 381–383.
- [32] P. Colombo, G. Mera, R. Riedel, G.D. Soraru, J. Am. Ceram. Soc. 93 (2010) 1805–1837.
- [33] R.M. Prasad, G. Mera, K. Morita, M. Müller, H.-J. Kleebe, A. Gurlo, M. Fasel, R. Riedel, J. Eur. Ceram. Soc. 32 (2012) 477–484.
- [34] M.S. Bazarjani, H.-J. Kleebe, M.M. Müller, C. Fasel, M.B. Yazdi, A. Gurlo, R. Riedel, Chem. Mater. 23 (2011) 4112–4123.
- [35] M. Wilhelm, M. Adam, M. Bäumer, G. Grathwohl, Adv. Eng. Mater. 10 (2008) 241–245.
- [36] M. Hojamberdiev, R.M. Prasad, K. Morita, M.A. Schiavon, R. Riedel, Micropor. Mesopor. Mat. 151 (2012) 330–338.
- [37] A. Gurlo, G. Miehe, R. Riedel, Chem. Commun. (2009) 2747–2749.
- [38] K.A. Michalow, D. Logvinovich, A. Weidenkaff, M. Amberg, G. Fortunato, A. Heel, T. Graule, M. Rekas, Catal. Today 144 (2009) 7–12.
- [39] S. Brunauer, P.H. Emmett, E. Teller, J. Am. Chem. Soc. 60 (1938) 309–319.
- [40] E.P. Barrett, L.G. Joyner, P.P. Halenda, J. Am. Chem. Soc. 73 (1951) 373–380.
- [41] K. Okada, N. Yamamoto, Y. Kameshima, A. Yasumori, K.J.D. MacKenzie, J. Am. Ceram. Soc. 84 (2001) 1591–1596.
- [42] G. Liu, F. Li, Z. Chen, G.Q. Lu, H.-M. Cheng, J. Solid State Chem. 179 (2006) 331–335.
- [43] M.A. Butler, J. Appl. Phys. 48 (1977) 1914–1920.
- [44] Y. Cong, J. Zhang, F. Chen, M. Anpo, J. Phys. Chem. C 111 (2007) 6976–6982.
- [45] X. Chen, C. Burda, J. Phys. Chem. B 108 (2004) 15446–15449.
- [46] E. György, A. Pérez del Pino, P. Serra, J.L. Morenza, Surf. Coat. Technol. 173 (2003) 265–270.
- [47] X. Chen, Y. Lou, A.C.S. Samia, C. Burda, J.L. Gole, Adv. Funct. Mater. 15 (2005) 41–49.
- [48] S. Andersson, B. Collen, U. Kuylenstierna, A. Magneli, Acta Chem. Scand. 11 (1957) 1641–1652.
- [49] L.A. Bursill, B.G. Hyde, O. Terasaki, D. Watanabe, Philos. Mag. 20 (1969) 347–359.
- [50] L.-M. Berger, J. Hard Mater. 3 (1992) 3–15.
- [51] T.P. Mernagh, R.P. Cooney, R.A. Johnson, Carbon 22 (1984) 39–42.
- [52] A.C. Ferrari, J. Robertson, Phys. Rev. B 61 (2000) 14095–14107.
- [53] M. Boutinguiza, B. Rodríguez-González, J. del Val, R. Comesaña, F. Lusquiños, J. Pou, Nanotechnology 22 (2011) 195606.
- [54] E. Ionescu, B. Papendorf, H.-J. Kleebe, R. Riedel, J. Am. Ceram. Soc. 93 (2010) 1783–1789.
- [55] S. Martínez-Crespiera, E. Ionescu, H.-J. Kleebe, R. Riedel, J. Eur. Ceram. Soc. 31 (2011) 913–919.
- [56] S. Adachi, Optical Properties of Crystalline and Amorphous Semiconductors: Materials and Fundamental Principles, Kluwer Academic Publishers, 1999.
- [57] T. Xu, L. Zhang, H. Cheng, Y. Zhu, Appl. Catal. B 101 (2011) 382–387.
- [58] Y. Hu, H.-L. Tsai, C.-L. Huang, J. Eur. Ceram. Soc. 23 (2003) 691–696.
- [59] J. Aguado, R. van Grieken, M.J. López-Muñoz, J. Marugán, Catal. Today 75 (2002) 95–102.
- [60] D.C. Hurum, A.G. Agrios, K.A. Gray, T. Rajh, M.C. Thurnauer, J. Phys. Chem. B 107 (2003) 4545–4549.
- [61] S.S. Barton, Carbon 25 (1987) 343–350.
- [62] M. Miyauchi, A. Ikezawa, H. Tobimatsu, H. Irie, K. Hashimoto, Phys. Chem. Chem. Phys. 6 (2004) 865–870.
- [63] Y. Ao, J. Xu, D. Fu, C. Yuan, Carbon 46 (2008) 596–603.
- [64] X. Wang, J.C. Yu, C. Ho, Y. Hou, X. Fu, Langmuir 21 (2005) 2552–2559.
- [65] H. Irie, Y. Watanabe, K. Hashimoto, J. Phys. Chem. B 107 (2003) 5483–5486.
- [66] T. Lindgren, J.M. Mwabora, E. Avendaño, J. Jonsson, A. Hoel, C.-G. Granqvist, S.-E. Lindqvist, J. Phys. Chem. B 107 (2003) 5709–5716.
- [67] T. Ihara, M. Miyoshi, Y. Iriyama, O. Matsumoto, S. Sugihara, Appl. Catal. B 42 (2003) 403–409.